Photocatalytic and Photocurrent Responses to Visible Light of the Lone-Pair-Based Oxysulfide $Sr_6Cd_2Sb_6S_{10}O_7$

Sandy Al Bacha[a,b,c], Sébastien Saitzek[a], Emma E. McCabe[c]*, Houria Kabbour[a]*

[a] Univ. Lille, CNRS, Centrale Lille, ENSCL, Univ. Artois, UMR 8181 – UCCS – Unité de Catalyse et Chimie du Solide, F-59000 Lille, France

[b] University of Kent, School of Physical Sciences, Canterbury, Kent CT2 7NH, U.K

[c] Durham University, Departement of Physics, Durham DH1 3LE, U.K.

Corresponding authors: emma.mccabe@durham.ac.uk , houria.kabbour@univ-lille.fr

ABSTRACT

We present a combined experimental and computational study on the recently reported oxysulfide $Sr_6Cd_2Sb_6S_{10}O_7$, to demonstrate its photocatalytic activity under solar irradiation. Our spectroscopy and photocurrent measurements, and tests for photocatalytic activity, indicate the potential of $Sr_6Cd_2Sb_6S_{10}O_7$ for photocatalytic applications. In particular, photoconduction measurements show a reproducible photocurrent of 1.25 $\mu A.cm^{-2}$ and indicate efficient electron-hole separation upon illumination. Density functional theory calculations, combined with crystal orbital Hamiltonian population analysis, give insights into the electronic structure of $Sr_6Cd_2Sb_6S_{10}O_7$ and the origin of its physical properties. Our comprehensive investigation into $Sr_6Cd_2Sb_6S_{10}O_7$ reveals the roles of its polar structure, polar Sb^{3+} coordination environments and the $5s^2$ lone pair in making this compound a potential candidate for solar water splitting photocatalysis.

INTRODUCTION

Photocatalysts, capable of splitting water for clean hydrogen production, are needed if we are to realize the potential of fuel cells (which combine hydrogen and oxygen to give electrical energy) to help meet the world's energy demands. For sustainable and clean hydrogen production, photocatalysts that are active under solar irradiation are needed, which limits the size of the band gap (1.23 - 3.1 eV). Oxide photocatalysts (e.g. TiO_2 (3.0 eV)[1], ZnO (3.2 eV)[2], $SrTiO_3$ (3.25 eV)[3]

and $ZnNb_2O_6$ (3.98 eV)[4]) typically have band gaps too large for excitation by visible light.[5] Making substitutions on the oxide sublattice, including introducing softer sulfide anions to give mixed-anion oxysulfide materials, is an effective strategy to tune the band gap to match the solar spectrum and give effective photocatalysis under visible light.[6,7] In addition to the size of the band gap, the H_2O/H_2 and O_2/H_2O redox potentials impose constraints on the valence band maximum (VBM) and conduction band minimum (CBM) for compatibility with for water splitting (a conduction band minimum more negative band than the reduction potential of H_2O/H_2 (0 V) and a valence band maximum more positive than the oxidation potential of O_2/H_2O (1.23 V)).[8]

A small number of oxysulfides have been highlighted as promising photocatalysts for water splitting under visible light including $Sm_2Ti_2S_2O_5$ with a 0.7% oxygen evolution activity[9], $LaOInS_2$[10] and α-$LaOInS_2$.[11] While some sulfides exhibit appropriate band gaps and photocatalytic activity, they suffer from sulfur self-oxidation (for instance $CuInS_2$). On the other hand, the introduction of O *2p* orbitals in the oxysulfides can stabilize the system, as demonstrated for $Y_2Ti_2O_5S_2$ with a band gap of 1.9 eV and an efficient stoichiometric production of H_2 and O_2.[12]

Beyond these basic requirements, much research is focused on optimizing the performance of photocatalytic materials but the key materials design features are not yet fully understood. One promising design strategy is to introduce polar units, with a built-in electric field, into the photocatalytic material to enhance electron-hole separation.[13,14,15] This polarization field facilitates the transfer of the photo-generated pairs to different active sites leading to an improved e^-/h^+ separation.[16] This enhanced charge carriers' separation can give better photoactivity,[17] (e.g. polar oxide $Na_3VO_2B_6O_{11}$).[18] Theory work has recently demonstrated the potential of heteroleptic and polar coordination environments in oxysulfides (in which the photoactive cation *M* is coordinated by both oxide and sulfide anions) to enhance photocatalytic performance, but this has not yet been explored experimentally.[19] A second feature that may be found in photocatalytic and photovoltaic materials is the presence of a (heavy) "lone pair" cation such as Bi^{3+}, Sb^{3+}, Sn^{2+}…[20,21,22] The presence of a $5s^2$ or $6s^2$ pone pair of electrons, and its energy relative to anion *p* orbitals, can determine the energy (and degree of delocalisation) of states at the top of the valence band which are key to explaining the optical response of these materials.[23,24]

The oxysulfide $Sr_6Cd_2Sb_6S_{10}O_7$ reported by Wang et al contains $5s^2$ Sb^{3+} cations in both homoleptic ($Sb(1)S_5$ and $Sb(3)O_3$) and heteroleptic ($Sb(2)OS_4$) coordination environments (figure

1a).[25] With a band gap of 1.89 eV and polar crystal structure, it has potential for photocatalytic behaviour. $Sr_6Cd_2Sb_6S_{10}O_7$ crystallizes in the polar space group *Cm* with a structure built up from zigzag $^2_\infty[CdSb_2OS_5]^{4-}$ layers. These zigzag layers are separated by pseudo-chains of $^1_\infty[Sb(3)O_{2.5}]^{2-}$ composed of [seesaw-shaped /C_{2v}] $[Sb(3)O_4]^{5-}$ units linked via their half-occupied (disorded) O(4) sites (figure 1a). The zigzag $^2_\infty[CdSb_2OS_5]^{4-}$ layers are built from $^1_\infty[CdS_3]^{4-}$ chains which are corner-linked to edge-shared chains of $^1_\infty[Sb(1)OS_3]^{3-}$ and $^1_\infty[Sb(2)OS_2]^{3-}$. Electronic structure calculations indicate that Sr, O and Cd contribute little to the band edges, whilst the Sb(1) and Sb(2) sites (and particularly the $5s^2$ pair from the $Sb(2)OS_4$ units) are responsible for the NLO activity.[25] Our combined experimental and computational study reported here allows us to investigate the relative importance of the anion in tuning the band gap and giving polar coordination environments, and the relationship with the Sb^{3+} $5s^2$ lone pair and its activity. Our studies demonstrate that $Sr_6Cd_2Sb_6S_{10}O_7$ has good photocatalytic performance, including under solar irradiation with efficient electron-hole separation. Insights from computational work confirms the key role of the $Sb(3)O_3$ entities with the greater lone pair stereoactivity whilst $Sb(1)S_5$ entities contribute most to the DOS just below the Fermi level (at the VBM) and thus to the band gap and the photocatalytic properties. During final preparation of this manuscript we became aware of a study of the oxyselenides analogue $Sr_6Cd_2Sb_6O_7Se_{10}$ and its photoelectric properties.[26] The findings of this recent study, including the roles of polar units of Sb^{3+} $5s^2$ lone pair, are consistent with our work, and complement our study by further showing how the anions *Q* in SbQ_5 units can tune the band-edge structure in these photoactive materials.

METHODS SECTION

A single-phase sample of $Sr_6Cd_2Sb_6S_{10}O_7$ (1 g) was synthesized by solid-state reaction from a stoichiometric mixture of the reagents SrS/CdS/Sb_2O_3/Sb/S (Alfa Aesar 99.5%). Because of the air sensitivity of some reagents, they were stored, weighed and ground together in an argon-filled glovebox. Reagent mixtures were then pressed into pellets and heated in an evacuated, sealed, carbon-coated quartz tube. The heat treatment consisted of heating to 700°C at a rate of 1.15°C/min dwelling for 48 h before cooling to room temperature in three hours. After this procedure a red powder was obtained.

X-ray powder diffraction (XRPD) pattern was collected on a Bruker D8 A25 diffractometer equipped with a Lynxeye XET linear detector (Cu Kα) in Bragg−Brentano geometry at room

temperature with a 1 s counting time and 0.02 ° step angle. Rietveld refinements using XRPD data were carried out using TopasAcademic software.[27,28] The background (shifted Chebyshev), sample height, lattice parameters, peak profiles (pseudo-Voight), atomic positions and atomic displacement parameters (a parameter for each atom type) were refined, as well as a correction for absorption due to surface roughness.[29]

Density functional theory (DFT) calculations were carried out using the projector-augmented-wave method[30] encoded in the Vienna *ab initio* simulation package (VASP)[31] and the generalized gradient approximation (GGA) of Perdew, Burke and Ernzerhof[32] for the exchange-correlation functionals. To deal with the structural disorder at the O(4) site, a (1×2×1) supercell is adopted which led to a disorder-free structure.[33,25] Full geometry optimizations were carried out using a plane-wave energy cutoff of 550 eV with k-points meshes (3×7×6) in the irreducible Brillouin zone. The relaxed structure was used for calculations of the electronic structure. The COHP (Crystal Orbital Hamilton Population) analysis was carried out in the framework of the LOBSTER software.[34,35,36]

The reflectance of the sample was measured from 200 to 900 nm using a PerkinElmer Lambda 650 spectrophotometer.

The photocurrents were collected using an electrochemical device (Autolab PGSTAT204, Metrohm) coupled to a LED module (LED driver kit, Metrohm). LEDs (450, 470, 505, 530, 590 and 627 nm) with low spectral dispersion are used. These LEDs are calibrated using a photodiode to determine the density of the luminous flux received by the sample. The photoelectrochemical measurements were performed in standard three-electrode cell (Magnetic Mount Photo-electrochemical Cell (Redox.me®), including Ag/AgCl and Pt wire acted as reference electrode and counter electrode, respectively. The cell used allows standardized illumination over 1 cm^2 by the rear face of the working electrode. The working electrode is made using the drop casting technique.[37] For this, the photocatalyst is dispersed in PVDF (PolyVinyliDene Fluoride) binder (with the 2:1 ratio), then deposited evenly on a ITO/glass substrate (Delta Technologies, Ltd). The electrolyte employed is an aqueous 0.1 M Na_2SO_4 solution.

The photocatalytic activity was determined by monitoring the degradation of Rhodamine B. The used photo-reactor consist of a 200 ml flask which is irradiated from above with a 40 W UV lamp (254 nm). An aluminum foil covers this unit to prevent exposure to UV radiations. Before any

measurements, the solution (containing 100 mL of Rhodamine B (2×10^{-6} mol dm^{-3}) and 100 mg of the photocatalyst powder ($Sr_6Cd_2Sb_6S_{10}O_7$) was stirred for 30 min in the dark to ensure an appropriate adsorption/desorption equilibrium. After this step, samples were taken, at regular intervals to monitor the evolution of the concentration of the photodegraded Rhodamine B by spectrophotometry. Absorbance measurements were carried out using a Shimadzu UV-2600 UV-visible spectrophotometer.

RESULTS

Rietveld analysis using high quality XRPD data collected for $Sr_6Cd_2Sb_6S_{10}O_7$ (figure 1b) was in good agreement with the model of *Cm* symmetry reported by Wang et al.[25]

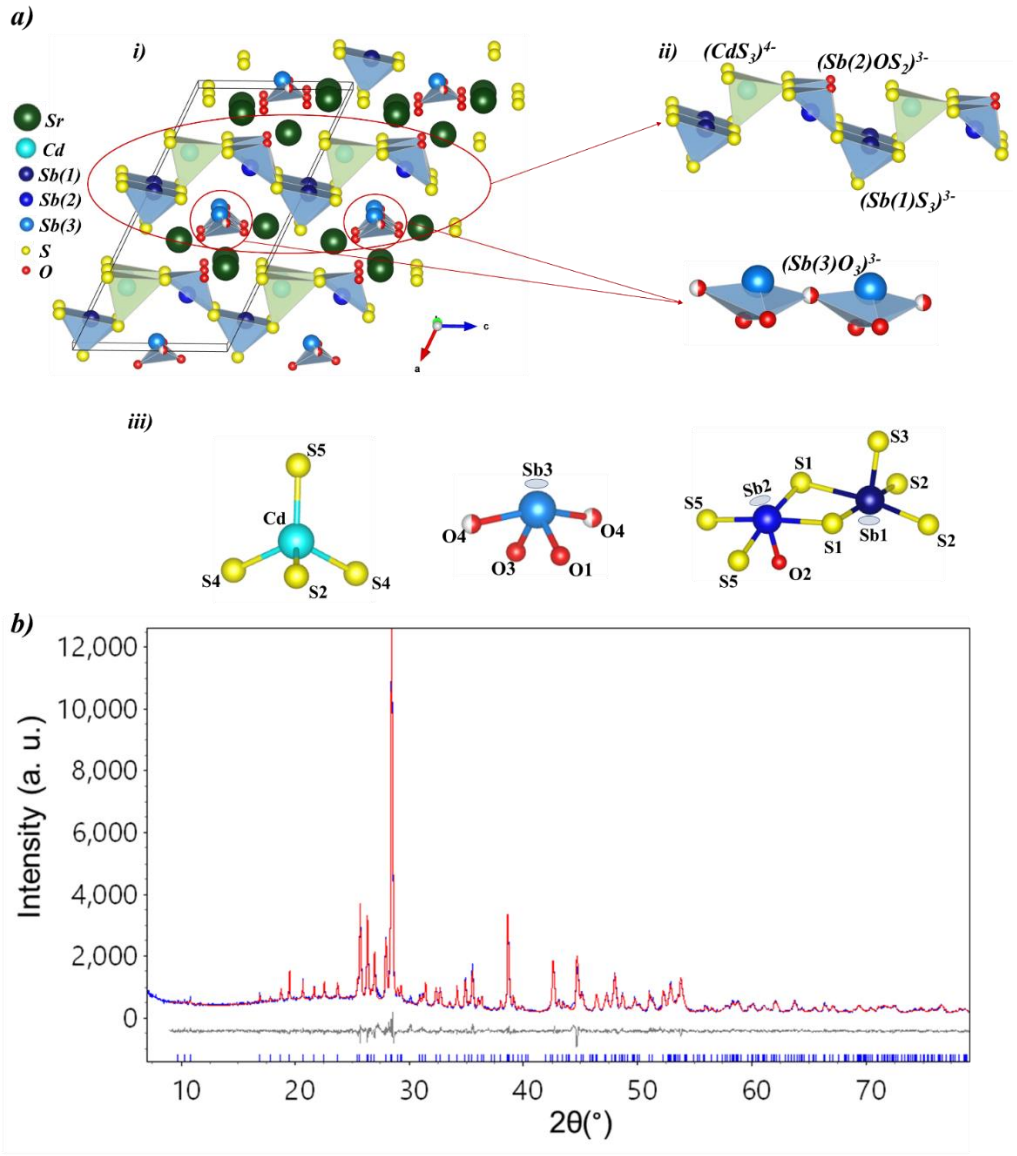

Figure 1: (a) (i) View of $Sr_6Cd_2Sb_6S_{10}O_7$. (ii) Zigzag layer formed of $[CdS_3]^{4-}$ tetrahedra and the mixed anion tetragonal pyramids of antimony $[SbOS_2]^{3-}$/$[SbS_3]^3$, pseudo-chains composed of $[Sb(3)O_3]^{3-}$ motifs joined by half-occupied O(4) vertices (iii) coordination environments of Cd and Sb ions. (b) Powder XRD Rietveld refinement profiles: the experimental (red) and the calculated (bleu) patterns are superimposed; the difference curve and Bragg positions are shown in gray and blue, respectively.

The magnitude and nature of the band gap of $Sr_6Cd_2Sb_6S_{10}O_7$ was measured by diffuse reflectance UV-visible spectroscopy. Figure 2a shows reflectance *vs*. wavelength for $Sr_6Cd_2Sb_6S_{10}O_7$. The reflectance data were analysed using the Kubelka-Munk function.[38] A Tauc plot (figure 2a) $[F(R)h\upsilon]^{1/n}$ *vs*. $[h\upsilon]$ (where $h\upsilon$ is the photon energy),[39] gives insight into the nature of the band gap: $Sr_6Cd_2Sb_6S_{10}O_7$ is reported to be an indirect bandgap semiconductor (hence n =

2) and a tangent to the inflection point on the Tauc plot gives an optical band gap E_g = 2.01(2) eV. This is in fairly close agreement with that reported by Wang *et al.* (1.89 eV).[25]

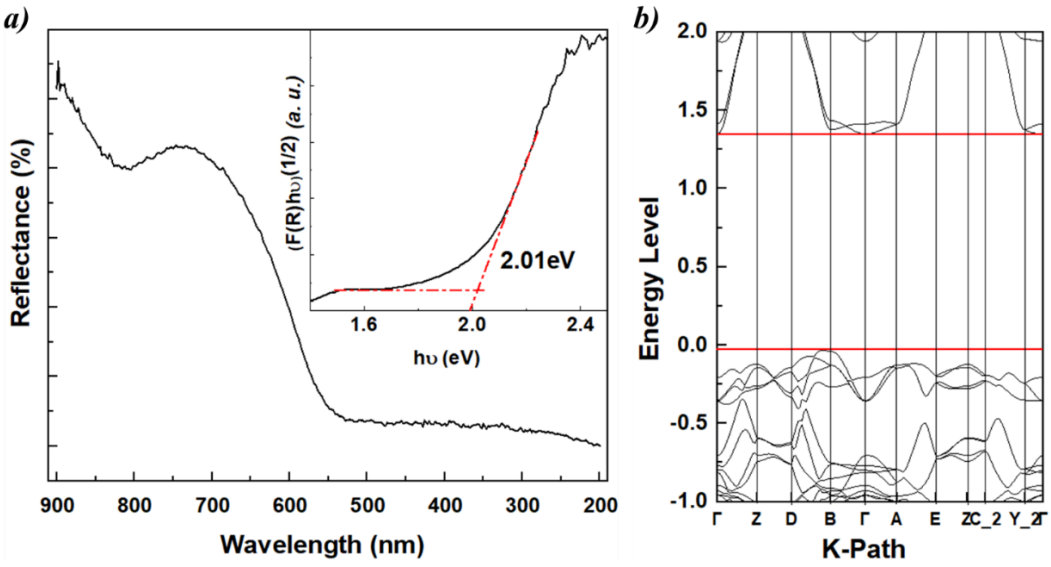

Figure 2 : (a) Diffuse-reflectance spectra with a Tauc plot inset to determine the experimental band gap. (b) Calculated band structure for $Sr_6Cd_2Sb_6S_{10}O_7$.

First principles Calculations. DFT calculations were carried out to investigate the electronic structure of $Sr_6Cd_2Sb_6S_{10}O_7$. The charge carriers' effective masses were computed from the band structure to gain insights into the mobility of the electron and holes and to probe the role of the Sb^{3+} lone pair. As a first step the structure was optimized using a supercell taking into account the disorder in the half-occupied O(4) site leading to the space group *Pc* for the resulting optimized structure. Calculations indicated an indirect band gap of 1.39 eV, slightly smaller than the experimental value, due to the well-known tendency of the GGA approximation (with PBE functional used here) to underestimate band gaps.[32] Figure 2b shows the calculated electronic band structure for $Sr_6Cd_2Sb_6S_{10}O_7$ with valence band maximum and conduction band minimum at Γ (0; 0; 0) and B (0; 0; 0.5) points, respectively.

In order to have a quantitative investigation of charge carriers, the effective masses of electrons (m^*_e) and of holes (m^*_h) were calculated[40] using the following equation near the CBM and the VBM:

$$\left(\frac{1}{m^*}\right)_{ij} = \frac{1}{\hbar^2}\frac{\partial^2 E_n(k)}{\partial k_i k_j} \qquad (1)$$

where $E_n(k)$ corresponds to the n^{-th} electronic band in *k*-space. Prior to the effective masses' extraction, the self-consistent electronic calculation was followed by a non-self-consistent calculation along the high symmetry lines with a fine spacing of 0.02 $Å^{-1}$ of *k*-points in reciprocal space. The band structure shows different dispersions of the bands at the CBM and VBM suggesting different mobility of electrons and holes. Since the VBM is located at Γ and the CBM at B, we investigated the directions $\Gamma \rightarrow B$ and $B \rightarrow D$ very near to the Γ or B points, both related to directions within the layers. In the meantime, we have investigated directions across the layers with $Y2 \rightarrow \Gamma$ for m_e^*.

The lowest value of $m_e^* = 0.218\ m_0$ was found for the electrons in the conduction band for intra-layer directions, while for interlayers we find much higher value of $m_e^* = 5.44\ m_0$. It shows the anisotropy of the charge carriers' mobility with easier transport within the layers as expected from the structure. Values below 0.5 m_0 (as found for electrons here) are usually considered as very low and indicative of a high mobility. As the mobility is inversely proportional to the effective mass this indicates a high electron mobility compared with other oxysulfides such as BiCuOS (0.59 m_0) and BiAgOS (0.68 m_0).[41] The hole mass was obtained by fitting bands at the valence band maximum and in contrast they are found to be heavier with a mass of 6.50 m_0 indicating a lower hole mobility compared to electrons, as expected. The difference in holes and electrons effective masses has the advantage of ensuring better separation of charge carriers and therefore a low rate of the electron-holes pairs recombination. These features make this compound attractive for efficient photoconduction.

The electron localization function (ELF) was also computed which gives insight into the nodal structure of the molecular orbitals. The ELF reflects localized electron pairs and allows us to investigate different bonds and lone pair electrons.[42] Looking at the local coordination geometry around the Sb^{3+} cations in figure 3, the distorted lone pair of antimony is clearly observed. As the environment of the antimony changes the Sb^{3+} $5s^2$ pair size changes, which indicates that the lone pair is sensitive to the O:S ratio, as expected based on the revised lone pair model.[43,44]

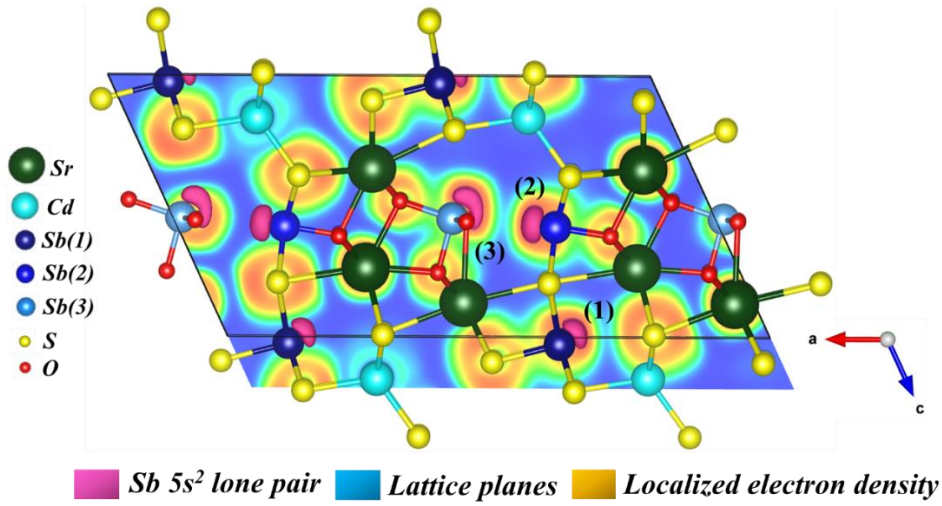

Figure 3 : DFT-computed ELF for the three different Sb coordination, $Sb(1)S_5$, $Sb(2)OS_4$ and $Sb(3)O_3$.

Based on the calculated electronic density and ELF, the Critic2 program[45,46] using the Yu and Trinkle (YT) method[47] was used to determine the critical points of the ELF and to obtain the electronic charge and volume within the basins (wells). Table 1 gathers the calculated positions, distances to the corresponding antimony atom, volumes and charges of the electronic lone pairs. The DFT calculated volume of the lone pairs has the trend SbO_3 > SbS_4O > SbS_5 indicating that the most ionic interactions lead to a greater stereoactivity as reported in previous studies.[48]

The calculated Sb-(LP) distances range from 0.823 Å for Sb1-LP1 (full sulfide coordination) to 1.142 Å for Sb3-LP3 (full oxide coordination) and with an intermediate distance of 0.875 Å for Sb2-LP2 (mixed anion coordination). The calculated electronic charges are 3.55 e^-, 3.77 e^- and 2.88 e^- for Sb1, Sb2 and Sb3 lone pairs, respectively. Despite its greater volume, the lower charge is found for Sb(3) in $Sb(3)O_3$. Charges reported with the same method are for instance reported by Poupon *et al.*: for oxotellurate (IV) compounds[49,50] for instance with a typical lone pair charge of 2.71 e^-. These findings reflect increasing delocalization of Sb^{3+} lone pair with increasing oxide coordination, consistent with DOS calculations reported for $Sr_6Cd_2Sb_6O_7Se_{10}$.[26]

We thus find that in this compound the $Sb(3)O_3$ contributes the most to the anisotropy and polarization field while $Sb(1)S_5$ contributes the most to the band edges which are both crucial for the photoconduction properties. It is also important to mention that we focus on a comparative analysis of the lone pairs within the title phase. One should also keep on mind that different

approaches to represent the Kohn-Sham orbitals may lead to different results if we consider the literature, therefore the comparison is not straightforward if not based on similar approaches.

Table 1. Description of the Lone Pairs: positions, Sb-E distances, charges and volumes.

Electronic lone pair	Position			Distance to Sb (Å)	Charge (e^-)	Volume (Å^3)
	x	*y*	*z*			
E1 (Sb(1)S5)	0.847(5)	0.25(3)	0.987(9)	0.823(2)	3.55(6)	20.44(4)
E2 (Sb(2)OS4)	0.340(4)	0.5(1)	0.562(6)	0.875(8)	3.37(4)	21.13(1)
E3 (Sb(3)O3)	0.420(2)	0.953(5)	0.475(8)	1.142(4)	2.88(9)	23.54(5)

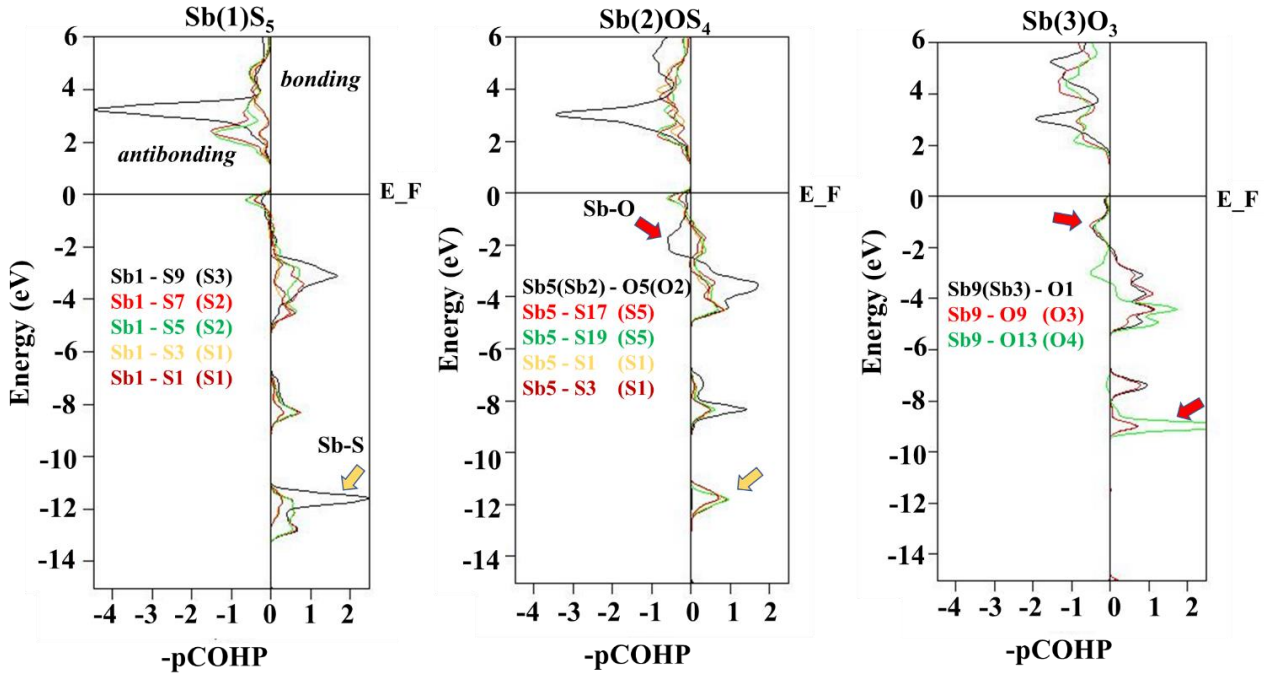

Figure 4 : COHP analysis for the bonds formed by $Sb(1)S_5$, $Sb(2)OS_4$ and $Sb(3)O_4$ (from left to right) with their ligands with the color codes indicated on the plots. The numbering of the atoms in the legend is that of the supercell in *P*1 used for the calculations (see SI).

Crystal Orbital Hamiltonian Population (COHP) has been also computed and pictures the bonding nature and strength, see figure 4. It is particularly interesting to focus on the top of the VBM where the states related to the lone pair formation are found as described for the PDOS. From

E_F down to about -2 eV/-3 eV, filled antibonding interactions between Sb 5*s* and S 3*p* and/or O 2*p* states are found. These interactions are responsible for the stereoactive lone pair which is consistent with the revised lone pair model.[43,44] Considering the different antimony sites, the $5s^2$ antibonding states for $Sb(1)S_5$ units remain relatively high in energy, immediately below the E_F (figure 4). In contrast, for $Sb(2)OS_4$ and $Sb(3)O_3$ sites with more O^{2-} anions in the Sb^{3+} coordination sphere, stronger Sb^{3+} $5s^2$ – O 2*p* hybridisation occurs. This gives increased stabilisation of Sb^{3+} $5s^2$ electrons (see the lower energy antibonding states between -2.0 and -3.5 eV) for the Sb(2) and Sb(3) sites, alongside increased localization (as discussed above from ELF analysis).

Photocatalytic activity. To quantify the photocatalytic efficiency of $Sr_6Cd_2Sb_6S_{10}O_7$, we carried out a study of the photodegradation of Rhodamine B by following the kinetics by UV-visible spectroscopy based on the maximum absorption of the dye (λ=565 nm). To describe the photocatalytic kinetics at the solid−liquid interface, the Langmuir−Hinshelwood (LH) model was used.[51] Taking an order 1 for the photodegradation reaction and plotting $Ln(C_0/C)$ vs. time to determine the apparent rate constant (k_{app}). Figure 5a shows the Langmuir-Hinshelwood kinetic plot for the first run of the $Sr_6Cd_2Sb_6S_{10}O_7$ photocatalyst. Despite a latency time of 20 min at the start of the reaction, a linear evolution with an apparent rate constant of $9.0\ .10^{-3}$ min^{-1} is observed, comparable with other photocatalysts (typically 10^{-2} min^{-1}),[52] indicating good kinetic performance of $Sr_6Cd_2Sb_6S_{10}O_7$. However, for an ideal photocatalyst, the degradation of Rhodamine (measured by the discoloration of the solution) should increase with time until it saturates at 100% when all the dye has been degraded. Photocatalysis by $Sr_6Cd_2Sb_6S_{10}O_7$ only gave 75 % degradation which may reflect instability of $Sr_6Cd_2Sb_6S_{10}O_7$ in these wet conditions (figure 5b), changes in surface structure or pollution of adsorption sites by reaction intermediates reducing efficiency; this has yet to be fully explored. Other lone pair-based materials, such as Bi_2WO_6 ($K_{app} = 6.3\times10^{-3}$ min^{-1}) and Bi_2MoO_6 ($K_{app} = 1.7\times10^{-3}$ min^{-1}) showed a 90% and 51% Rhodamine B degradation, respectively.[53] Despite the greater lone pair activity of Bi^{3+} based materials, their capacity to photodegrade the Rhodamine B is comparable to $Sr_6Cd_2Sb_6S_{10}O_7$ with lower lone pair activity. This suggests that whilst a higher stereochemical activity might reduce the electronic band gap,[54,55] its influence on the rate of the photodegradation is difficult to compare directly as several other structural parameters may play a role (including polarity). Meanwhile, microstructure and the morphology

of the semiconductor, and its stability in the electrolyte, are also likely to influence the rate of degradation.

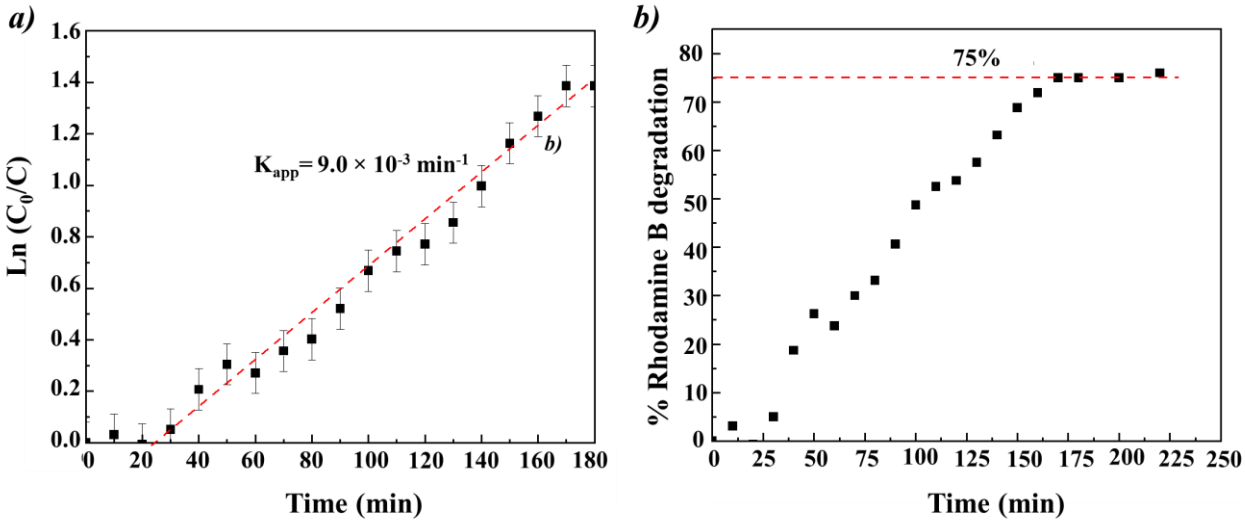

Figure 5 : (a) Langmuir-Hinshelwood kinetic plot for the degradation of Rhodamine B on $Sr_6Cd_2Sb_6S_{10}O_7$. (b) Percentage of discoloration of Rhodamine B on $Sr_6Cd_2Sb_6S_{10}O_7$ photocatalyst.

Photocurrent Measurements. The chronoamperometry measurements (current density variation Δj between illumination and dark cycles) achieved on $Sr_6Cd_2Sb_6S_{10}O_7$ film for a 0.4 V bias voltage and under an excitation of 450 nm is presented in the figure 6a. A significant change in transient photocurrent is observed when the underside of the working electrode is illuminated: the photocurrent generated increases from 0.65 to 0.95 µA.cm^{-2} for a power density of 22 to 111 mW.cm^{-2}, respectively. The photocurrent generated increases with the intensity of the luminous flux according to a classical power law[56] (figure 6b). The power law fitting gives a curve going through the origin with an equation of $\Delta j=3.52\times10^{-1}\phi^{0.208}$. The value of the exponent provides the information of traps present in the sample. Indeed, for an ideal trap-free system, the exponent is equal to 1 and the photocurrent scales linearly with the illumination power. But for trap states, the exponent becomes smaller than 1 (as for high powers most of the traps are already filled in and further illumination power cannot effectively increase the photogain).[57] Thus, in the present case, the low value of the exponent indicates the presence of many traps in the compound. The photocurrent response (figure 6a) shows also a characteristic decay from a "spike" to a steady state during illumination. The presence of this spike is explained by the rapid separation of the

electron/hole pairs under illumination, then the establishment of an equilibrium state between the recombination and the transfer of the carriers. Parkinson *et al* .[58] proposed a model making it possible to determine the transfer and recombination constants from the modeling of the exponential decrease of this current peak. Based on this model and for ϕ_0=111 mW.cm^{-2}, we can deduce that the transfer and recombination constants are 0.25 and 0.08 min^{-1}, respectively (i.e. a transfer efficiency of 78 % figure 4 SI).

In addition, the transient photocurrent response for V_{bias}=0.4 V vs. wavelength is shown in figure 6c. The highest photocurrent is observed for an irradiation at 450 nm and lower photocurrents are observed for longer wavelength (lower energy) irradiation. This is consistent with the decrease in absorbance observed on the Tauc plot (figure 2).

The previous tests were also performed under the same excitation of 450 nm but this time for a 0 V bias voltage on the $Sr_6Cd_2Sb_6S_{10}O_7$ film, and a clear reproducible photocurrent was observed (figure 5a SI). Between different illumination and dark cycles, the generated photocurrent increased with the intensity of the luminous flux from 0.045 to 0.95 µA.cm^{-2}, according to a classical power law. Although the characteristic 'spike' shape of the peaks (observed at 0.4 V bias voltage, figure 6) was lost, the exponent we obtained in this case is higher (0.471), indication of a decrease in the trap states (figure 5b SI). A higher photocurrent response is also observed at 450 nm (0.065 µA.cm^{-2}) and lower values occurred at longer wavelengths (figure 5c SI), similar to the transient photocurrent response for the 0.4 V voltage with the variation of the wavelengths.

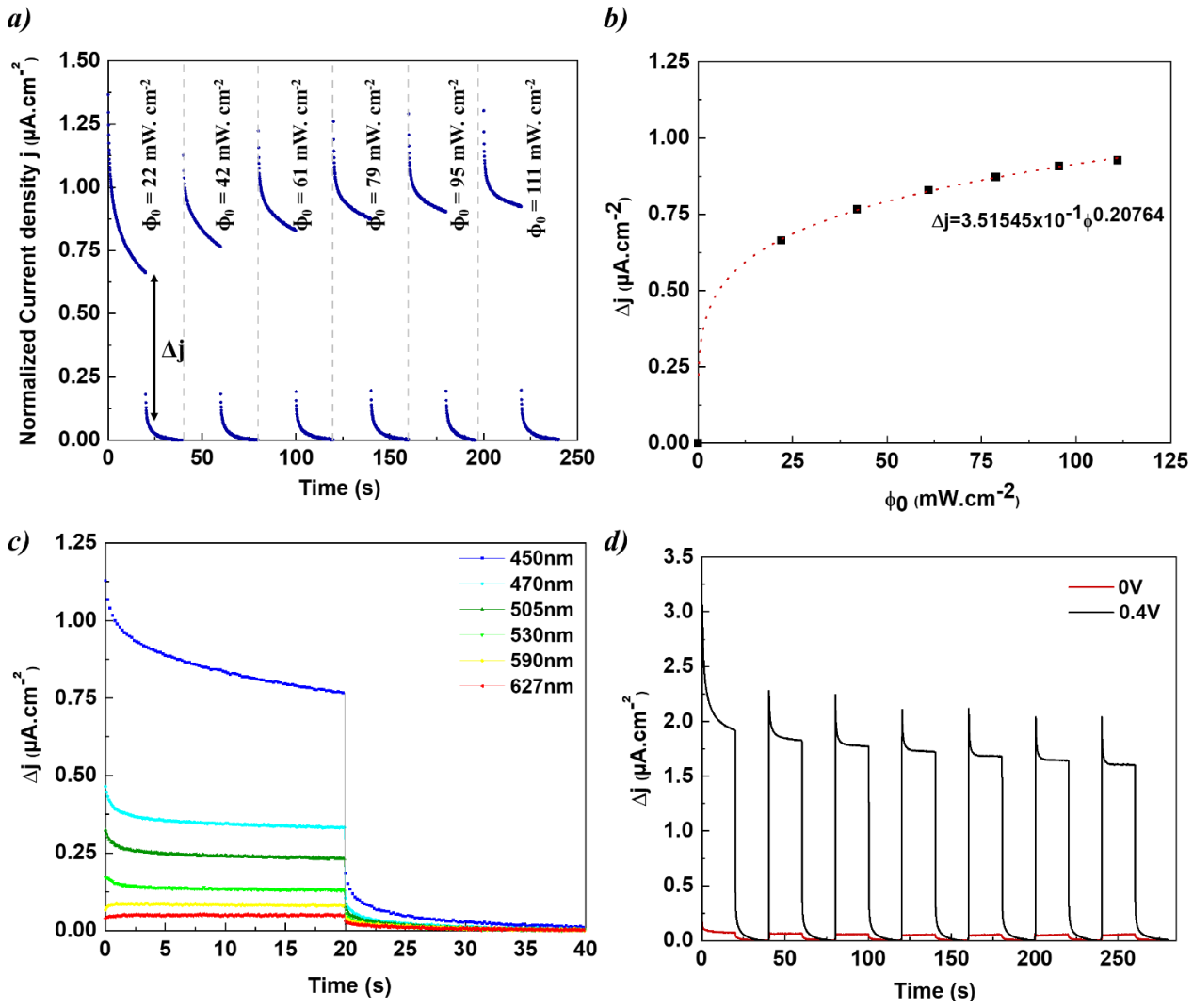

Figure 6 : (a) Transient photocurrent response (V_{bias}=0.4 V under a 450 nm excitation) of $Sr_6Cd_2Sb_6S_{10}O_7$ (b) Evolution of the photocurrent density the power density of light (c) Transient photocurrent response vs. wavelengths (constant light intensity ϕ_0=42 mW cm^{-2}) of $Sr_6Cd_2Sb_6S_{10}O_7$ (d)) Transient photocurrent response under solar illumination (100 mW.cm^{-2}) for V_{bias}=0.4 V and V_{bias}=0V.

The transient photocurrent response under solar illumination (150 W Xenon lamp with AM 1.5G filter – 100 mW.cm^{-2}) was also measured by carrying out on/off cycles (figure 6d). For a bias voltage of 0.4 V, we can see a slight decrease in the value of the generated photocurrent. This remains more stable when no potential is applied (red curve). This decrease indicates a photocorrosion phenomenon which may be due to a material or chemical instability within the electrolyte used. The kinetics of the transient photocurrent evolves between 0 V and 0.4 V (figure 6 SI), without applied potential the kinetics is slow and does not show a spike. This behavior can

be explained by the carrier trapping effect induce by surface defects.[59] While at higher potentials de-trapping is facilitated by the induced electric field.

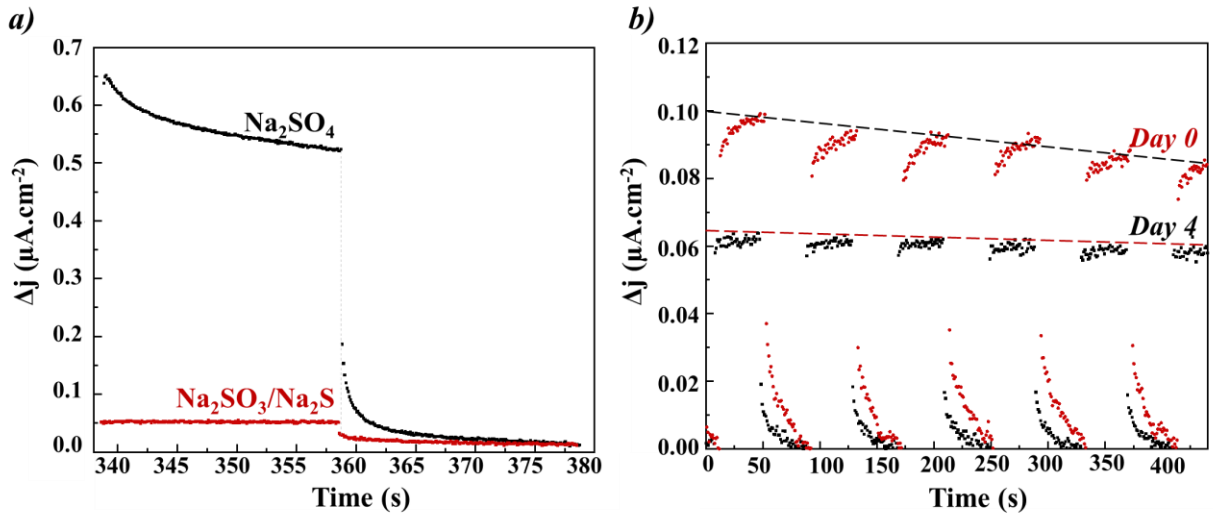

Figure 7 : (a) Electrolyte influence (Na_2SO_4, Na_2SO_3/Na_2S) on the transient photocurrent response of $Sr_6Cd_2Sb_6S_{10}O_7$ (b) Transient photocurrent response of $Sr_6Cd_2Sb_6S_{10}O_7$ in Na_2SO_3/Na_2S electrolyte on Day0 and Day4.

To further understand the degradation described above in Na_2SO_4 electrolyte, we considered other electrolyte solutions, including a mixture of 0.1 M Na_2SO_3 and 0.01 M Na_2S in order to stabilize the oxysulfide phase by the presence of S^{2-} ions. In addition, sulfite anions are hole scavengers that can prevent photocorrosion.[60] Although the photocurrent was lower for this Na_2SO_3/Na_2S electrolyte (figure 7a) the film was stable even over four days (figure 7b), indicating a significant reduction in photocorrosion compared with in the Na_2SO_4 electrolyte. To complete, the stability of the phase with respect to pH was studied but this led to degradation of $Sr_6Cd_2Sb_6S_{10}O_7$ (detected by XRPD analysis see figure 7 SI) for acid or basic solution, thus confirming a degradation of the oxysulfide in aqueous medium as observed in the photocatalysis experiments.

The Mott-Schottky (MS) plot of $1/C^2$ *vs.* applied potential (figure 8a) indicates the conduction type, the concentration of the charge carriers (N) and the flat band potential (E_{fb}).[52] The n-type semiconducting behavior is confirmed by the positive slope with a flat band potential E_{fb} estimated to be -0.46(1) V *vs.* Ag/AgCl (reference electrode) or 0.13(2) V *vs.* RHE (reversible hydrogen electrode). This estimated position of the flat band potential gives insight into the position of the CB or VB band edge depending on the conduction behavior.[61] The flat band potential reflects the

position of the Fermi level which lies close to the conduction band minimum (CBM) ~ 0.1 in a n-type semiconductor.[62] This calculated value is close to the calculated CB band edge position (figure 8b) using the empirical method based on Mulliken electronegativities proposed by Butler and Ginley[63] and further described by Xu and Schoonen,[64] using the following equation:

$$E_{VB,CB} = E_0 + \prod_{M=1}^{n} \chi_M^{j\ 1/n} \pm E_{gap}/2 \qquad (2)$$

where $E_{VB,CB}$ corresponds to the positions of the valence and conduction band edges; E_0 to the difference between (NHE) and the vacuum (E_0 = -4.5 eV); χ_M is the electronegativity of the atom M in the Mulliken scale with *n* the number of atoms and *j* the stochiometric ratio. Such calculations for the band edge positions were reported in a study by Castelli *et al.*[65] which compares a number of photocatalysts. We've used this method here to confirm that the band edge positions of $Sr_6Cd_2Sb_6S_{10}O_7$ encompass the redox potential of water, an essential requirement for photocatalytic water splitting.

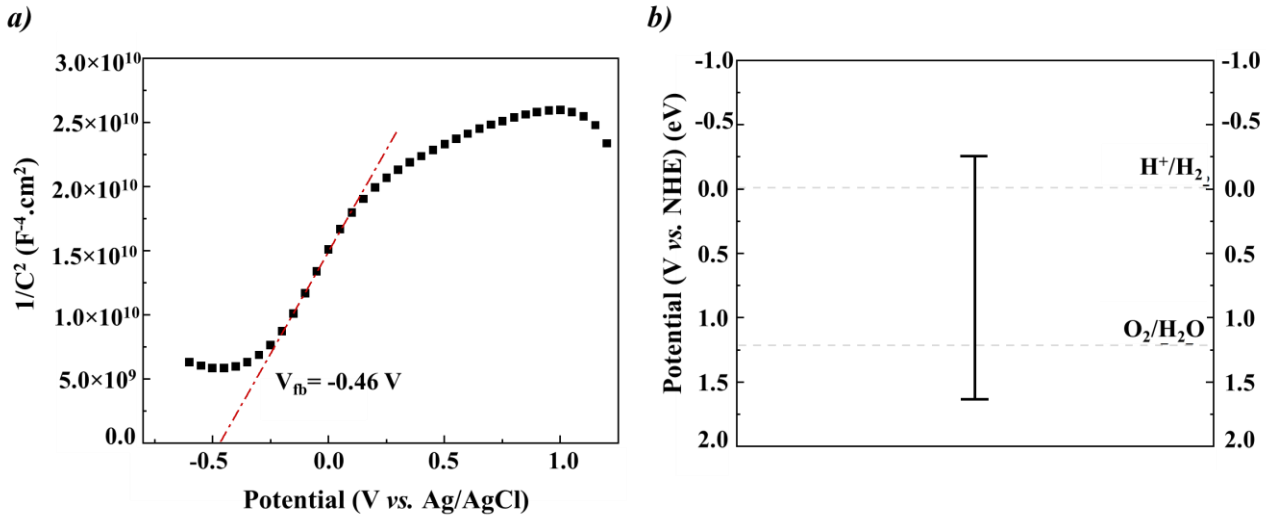

Figure 8 : (a) Mott-Schottky plot for $Sr_6Cd_2Sb_6S_{10}O_7$ deposited on ITO/Glass performed at 1000 Hz. (b) Calculated band edges positions for $Sr_6Cd_2Sb_6S_{10}O_7$; The levels of H_2 and O_2 evolution are indicated by dashed lines.

DISCUSSION

Many of the features of $Sr_6Cd_2Sb_6S_{10}O_7$ highlighted by Wang *et al.*, including the mixed-anion coordination environments of Sb^{3+} cations, its polar structure, and the presence of stereochemically-active lone pairs of electrons,[25] suggested the potential for $Sr_6Cd_2Sb_6S_{10}O_7$ to

show photocatalytic activity. Wang *et al*. found that the VBM and CBM in $Sr_6Cd_2Sb_6S_{10}O_7$ are composed primarily of S 3*p* and Sb 5*s*, 5*p* states, or Sb 5*p* states, respectively, giving an optical band gap of 1.89 eV.[25] This is much lower than the band gap in antimony oxides such as α-Sb_2O_3 (3.38 eV), β-Sb_2O_3 (2.25 eV), γ-Sb_2O_3 (2.55 eV), α-Sb_2O_4 (1.89 eV) and β-Sb_2O_4 (2.10 eV),[66] highlighting the potential to tune band gaps by including anions from different rows of the periodic table in mixed-anion systems, as in oxysulfides. This explains the functionality of $Sr_6Cd_2Sb_6S_{10}O_7$ under solar irradiation, including its photocatalytic activity (figures 5 and 6). However, the presence of oxide and sulfide anions alone isn't sufficient for a photocurrent response under sunlight irradiation, and both $[(Ba_{19}Cl_4)(Ga_6Si_{12}O_{42}S_8)]$ and $LaGaS_2O$, with heteroleptic Ga^{3+} coordination environments, require irradiation by higher-energy UV light before a photocurrent response is observed.[67,68]

A key feature in the photocatalytic activity of $Sr_6Cd_2Sb_6S_{10}O_7$ is the $5s^2$ lone pair on Sb^{3+} sites. Corey *et al*.,[69] and more recently Wang *et al.*[24] have shown that the stereochemical activity of the Sb^{3+} $5s^2$ lone pair increases with increasing electronegativity of the chalcogenide in the binary chalcogenides Sb_2Q_3 (Q = O, S, Se, Te).[69,24] This is consistent with ELF and COHP analysis (figure 3 and 4) (and with the *R* factors reflecting stereochemical activity[70] determined in this work, see supporting information) for the $Sb(1)S_5$, $Sb(2)OS_4$ and $Sb(3)O_3$ sites in $Sr_6Cd_2Sb_6S_{10}O_7$. The stereochemical activity is comparable to that reported for arsenic sulfides (typically 0.59 – 0.73)[71] but lower than that reported for bismuth oxides[70] with smaller energy difference between cation ns^2 and anion valence *n*p orbitals. The Sb^{3+} $5s^2$ lone pair contributes to the density of states at the top of the valence band, thus playing a key role in reducing the band gap towards the energy of solar irradiation, and the extent of its stereochemical activity is reflected in the energy range of these states.[24]

$Sr_6Cd_2Sb_6S_{10}O_7$ contains antimony cations in both homoleptic environments ($Sb(1)S_5$ and $Sb(3)O_3$ sites) and heteroleptic environments ($Sb(2)OS_4$). The driving forces for significant anion-segregation in oxysulfides (giving predominantly homoleptic cation coordination and often layered structures) *vs* more mixing of anions and heteroleptic coordination environments are not fully explored, but may relate to the relative softness/hardness of the specific combination of cations and anions.[72] It's striking that a strong electron-hole separation is indicated by the shape of the photocurrent response in both $Sr_6Cd_2Sb_6S_{10}O_7$ (figure 6) and $LaGaS_2O$.[68] It has been proposed that

polar aspects to the structure enhance electron-hole separation in oxysulfides[19] and comparison of these two systems can be instructive. Both have polar coordination environments for the photoactive cations. In $Sr_6Cd_2Sb_6S_{10}O_7$ this is due to the stereochemical activity of the $5s^2$ lone pair favouring lower-symmetry sites, with the polarity decreasing with increasing sulfide coordination.[25] By contrast, the polar symmetry (*m*, or *C*s) of the Ga^{3+} sites (with [Ar] electron configuration) in $LaGaS_2O$ arises as a result of its heteroleptic $[GaO_2S_2]^{-5}$ coordination.[68] However, these two photocatalytic oxysulfides differ in that $Sr_6Cd_2Sb_6S_{10}O_7$ adopts a polar crystal structure (of *Cm* symmetry)[25] whilst $LaGaS_2O$ crystallises with a non-polar structure (of *Pbcm* symmetry).[68] This comparison suggests that a polar coordination environment around the photo-active cation may play a greater role in enhancing electron-hole separation than the presence of a polar axis in the crystal structure.

Comparison of the results presented above for $Sr_6Cd_2Sb_6S_{10}O_7$ and the recently reported oxyselenide analogue $Sr_6Cd_2Sb_6O_7Se_{10}$[26] reveal that both compounds have indirect band gaps, with a slightly smaller gap (1.55 eV) for the 'softer' oxyselenide (compared with 1.89 eV for the oxysulfide). A much higher photocurrent response (50 $\mu A.cm^{-2}$ under 700 nm excitation and Bias = 5 V) was measured for $Sr_6Cd_2Sb_6O_7Se_{10}$ than for $Sr_6Cd_2Sb_6S_{10}O_7$ (0.95 $\mu A.cm^{-2}$ under a 450 nm excitation, figure 6 and figure 5a SI). This difference can be attributed to the higher bias voltage (5 V) used for measurements on the oxyselenide (compared with bias voltage of 0.4 and 0 V used for measurements on $Sr_6Cd_2Sb_6S_{10}O_7$ reported above), as higher responses are typically observed with increasing voltage. The good photoelectric performances due to the efficient charge carriers' separation in both analogues can be explained by the presence of a strong polarization within the sublattices because of the large dipole moments of the polar Sb units. Slightly higher dipole moments were calculated in the case of the oxysulfide ($[SbOS_4]^{7-}$ 15.5 D > $[SbS_5]^{7-}$ 12.7 D),[25] lower ones were found in the oxyselenide, $[SbOSe_4]^{7-}$ 15 D > $[SbSe_5]^{7-}$ 11.9 D, which can explain the difference in the photocurrent peak shape, and therefore in the kinetics of the charge carriers' separation for $Sr_6Cd_2Sb_6S_{10}O_7$ and $Sr_6Cd_2Sb_6O_7Se_{10}$, although both compounds demonstrated a slow recombination rate.

CONCLUSION

In this paper, we highlight the potential of the oxysulfide $Sr_6Cd_2Sb_6S_{10}O_7$ for water-splitting photocatalysis, including under solar irradiation, Many features that contribute to its non-linear

optical properties such as the presence of stereochemically-active lone pairs and the combination of anions to tune orbital energies[25] are also relevant for designing photocatalytic materials. Our combined experimental and computation investigation demonstrates that the mixed-anion nature of the oxysulfides is effective in tuning the band gap of these systems, but is also important for tuning the stereochemical activity of lone pairs electrons and hence the photocatalytic properties. A key challenge in designing useable photocatalysts is to limit the charge carriers' recombination which competes with the desired water-splitting redox reactions. It is striking to observe the photocurrent response in $Sr_6Cd_2Sb_6S_{10}O_7$ that is typical of a material with very efficient electron-hole separation and migration. This is supported by DFT calculations which indicate different mobility for electrons and holes, and very mobile electrons (with an effective mass below 0.5 m_0). Our theoretical study shows that antibonding interactions involving Sb^{3+} 5*s* and anion n*p* states are responsible for the DOS just below the Fermi level and for the stereochemical activity of the $5s^2$ lone pair – with its stereochemical activity sensitive to the O/S ratio in the Sb coordination environment. We thus identify the $Sb(3)O_3$ entity as the most polar Sb site, contributing the most to the polar nature and enhancing electron-hole separation, whilst $Sb(1)S_5$ entities contribute most to the DOS at the VBM. The study demonstrates the importance of lone pairs in designing photocatalytic (and likely photovoltaic) materials, and the balance between the cation site polarity and energies of cation valence states that can be tuned by anion substitution. Further work to optimise film deposition and operating conditions are underway.

ASSOCIATED CONTENT

Supporting Information. The supporting Information is available free of charge.

Additional experimental details related to the stereochemical activity calculation and photocurrent measurements; refinement details from Rietveld refinement of $Sr_6Cd_2Sb_6S_{10}O_7$ using room temperature XRPD data; unit cell parameters and atomic coordinates of the optimized structure (PDF).

ACKNOWLEDGMENTS

I-Site (ULNE), University of Lille and University of Kent are thanked for cotutelle funding (S. Al Bacha). Durham University is thanked for hosting research visit. Dr. Donna Arnold is thanked for helpful discussions. This study was supported by the French government through the Programme

Investissement d'Avenir (I-SITE ULNE / ANR-16-IDEX-0004 ULNE) managed by the Agence Nationale de la Recherche (Project ANION-COMBO). X-Rays Diffractometers are funded by Région NPDC, FEDER, CNRS and MESR. The regional computational cluster supported by Lille University, CPER Nord-Pas-de-Calais/CRDER, France Grille CNRS and FEDER is thanked for providing computational resources.

REFERENCES

(1) Hashimoto, K.; Irie, H.; Fujishima, A. TiO2 Photocatalysis: A Historical Overview and Future Prospects. *Jpn. J. Appl. Phys.* **2005**, *44* (12R), 8269.
(2) Maruska, H. P.; Ghosh, A. K. Photocatalytic Decomposition of Water at Semiconductor Electrodes. *Sol. Energy* **1978**, *20* (6), 443–458.
(3) Van Benthem, K.; Elsässer, C.; French, R. Bulk Electronic Structure of SrTiO 3: Experiment and Theory. *J. Appl. Phys.* **2001**, *90* (12), 6156–6164.
(4) Ji, S. M.; Choi, S. H.; Jang, J. S.; Kim, E. S.; Lee, J. S. Band Gap Tailored Zn (Nb1− x V x) 2O6 Solid Solutions as Visible Light Photocatalysts. *J. Phys. Chem. C* **2009**, *113* (41), 17824–17830.
(5) Maeda, K.; Domen, K. New Non-Oxide Photocatalysts Designed for Overall Water Splitting under Visible Light. *J. Phys. Chem. C* **2007**, *111* (22), 7851–7861.
(6) Cui, J.; Li, C.; Zhang, F. Development of Mixed-Anion Photocatalysts with Wide Visible-Light Absorption Bands for Solar Water Splitting. *ChemSusChem* **2019**, *12* (9), 1872–1888.
(7) Goto, Y.; Seo, J.; Kumamoto, K.; Hisatomi, T.; Mizuguchi, Y.; Kamihara, Y.; Katayama, M.; Minegishi, T.; Domen, K. Crystal Structure, Electronic Structure, and Photocatalytic Activity of Oxysulfides: La2Ta2ZrS2O8, La2Ta2TiS2O8, and La2Nb2TiS2O8. *Inorg. Chem.* **2016**, *55* (7), 3674–3679.
(8) Kong, D.; Zheng, Y.; Kobielusz, M.; Wang, Y.; Bai, Z.; Macyk, W.; Wang, X.; Tang, J. Recent Advances in Visible Light-Driven Water Oxidation and Reduction in Suspension Systems. *Mater. Today* **2018**, *21* (8), 897–924.
(9) Ishikawa, A.; Takata, T.; Kondo, J. N.; Hara, M.; Kobayashi, H.; Domen, K. Oxysulfide Sm2Ti2S2O5 as a Stable Photocatalyst for Water Oxidation and Reduction under Visible Light Irradiation (Λ≤ 650 Nm). *J. Am. Chem. Soc.* **2002**, *124* (45), 13547–13553.
(10) Miura, A.; Oshima, T.; Maeda, K.; Mizuguchi, Y.; Moriyoshi, C.; Kuroiwa, Y.; Meng, Y.; Wen, X.-D.; Nagao, M.; Higuchi, M. Synthesis, Structure and Photocatalytic Activity of Layered LaOInS 2. *J. Mater. Chem. A* **2017**, *5* (27), 14270–14277.
(11) Kabbour, H.; Sayede, A.; Saitzek, S.; Lefevre, G.; Cario, L.; Trentesaux, M.; Roussel, P. Structure of the Water-Splitting Photocatalyst Oxysulfide α-LaOInS 2 and Ab Initio Prediction of New Polymorphs. *Chem. Commun.* **2020**, *56* (11), 1645–1648.
(12) Wang, Q.; Nakabayashi, M.; Hisatomi, T.; Sun, S.; Akiyama, S.; Wang, Z.; Pan, Z.; Xiao, X.; Watanabe, T.; Yamada, T. Oxysulfide Photocatalyst for Visible-Light-Driven Overall Water Splitting. *Nat. Mater.* **2019**, *18* (8), 827–832.
(13) Dong, X.-D.; Zhang, Y.-M.; Zhao, Z.-Y. Role of the Polar Electric Field in Bismuth Oxyhalides for Photocatalytic Water Splitting. *Inorg. Chem.* **2021**, *60* (12), 8461–8474.
(14) Lou, Z.; Wang, P.; Huang, B.; Dai, Y.; Qin, X.; Zhang, X.; Wang, Z.; Liu, Y. Enhancing Charge Separation in Photocatalysts with Internal Polar Electric Fields. *ChemPhotoChem* **2017**, *1* (5), 136–147.
(15) Dong, X.-D.; Yao, G.-Y.; Liu, Q.-L.; Zhao, Q.-M.; Zhao, Z.-Y. Spontaneous Polarization Effect and Photocatalytic Activity of Layered Compound of BiOIO3. *Inorg. Chem.* **2019**, *58* (22), 15344–15353.

(16) Chen, F.; Huang, H.; Guo, L.; Zhang, Y.; Ma, T. The Role of Polarization in Photocatalysis. *Angew. Chem. Int. Ed.* **2019**, *58* (30), 10061–10073.
(17) Guo, Y.; Shi, W.; Zhu, Y. Internal Electric Field Engineering for Steering Photogenerated Charge Separation and Enhancing Photoactivity. *EcoMat* **2019**, *1* (1), e12007.
(18) Chen, J.; Zhai, Y.; Yu, Y.; Luo, J.; Fan, X. Spatial Separation of Photo-Induced Charge Carriers in a Na3VO2B6O11 Polar Material and Its Enhanced Photocatalytic Activity. *Appl. Surf. Sci.* **2021**, *556*, 149809.
(19) Vonrüti, N.; Aschauer, U. Band-Gap Engineering in AB (O x S 1− x) 3 Perovskite Oxysulfides: A Route to Strongly Polar Materials for Photocatalytic Water Splitting. *J. Mater. Chem. A* **2019**, *7* (26), 15741–15748.
(20) Ok, K. M. Functional Layered Materials with Heavy Metal Lone Pair Cations, Pb 2+, Bi 3+, and Te 4+. *Chem. Commun.* **2019**, *55* (85), 12737–12748.
(21) Handy, J. V.; Zaheer, W.; Rothfuss, A. R.; McGranahan, C. R.; Agbeworvi, G.; Andrews, J. L.; García-Pedraza, K. E.; Ponis, J. D.; Ayala, J. R.; Ding, Y. Lone but Not Alone: Precise Positioning of Lone Pairs for the Design of Photocatalytic Architectures. *Chem. Mater.* **2022**.
(22) Suzuki, H.; Kunioku, H.; Higashi, M.; Tomita, O.; Kato, D.; Kageyama, H.; Abe, R. Lead Bismuth Oxyhalides PbBiO2X (X= Cl, Br) as Visible-Light-Responsive Photocatalysts for Water Oxidation: Role of Lone-Pair Electrons in Valence Band Engineering. *Chem. Mater.* **2018**, *30* (17), 5862–5869.
(23) Kavanagh, S. R.; Savory, C. N.; Scanlon, D. O.; Walsh, A. Hidden Spontaneous Polarisation in the Chalcohalide Photovoltaic Absorber Sn 2 SbS 2 I 3. *Mater. Horiz.* **2021**, *8* (10), 2709–2716.
(24) Wang, X.; Li, Z.; Kavanagh, S. R.; Ganose, A. M.; Walsh, A. Lone Pair Driven Anisotropy in Antimony Chalcogenide Semiconductors. *ArXiv Prepr. ArXiv210908117* **2021**.
(25) Wang, R.; Liang, F.; Wang, F.; Guo, Y.; Zhang, X.; Xiao, Y.; Bu, K.; Lin, Z.; Yao, J.; Zhai, T. Sr6Cd2Sb6O7S10: Strong SHG Response Activated by Highly Polarizable Sb/O/S Groups. *Angew. Chem. Int. Ed.* **2019**, *58* (24), 8078–8081.
(26) Wang, R.; Wang, F.; Zhang, X.; Feng, X.; Zhao, C.; Bu, K.; Zhang, Z.; Zhai, T.; Huang, F. Improved Polarization in the Sr6Cd2Sb6O7Se10 Oxyselenide through Design of Lateral Sublattices for Efficient Photoelectric Conversion. *Angew. Chem.* **2022**.
(27) Coelho, A. A. TOPAS and TOPAS-Academic: An Optimization Program Integrating Computer Algebra and Crystallographic Objects Written in C++. *J. Appl. Crystallogr.* **2018**, *51* (1), 210–218.
(28) Coelho, A. TOPAS Academic: General Profile and Structure Analysis Software Fo r Powder Diffraction Datafile, 5th Editio. *Karlsr. Ger.* **2012**.
(29) Pitschke, W.; Hermann, H.; Mattern, N. The Influence of Surface Roughness on Diffracted X-Ray Intensities in Bragg–Brentano Geometry and Its Effect on the Structure Determination by Means of Rietveld Analysis. *Powder Diffr.* **1993**, *8* (2), 74–83.
(30) Kresse, G.; Joubert, D. From Ultrasoft Pseudopotentials to the Projector Augmented-Wave Method. *Phys. Rev. B* **1999**, *59* (3), 1758.
(31) Sun, G.; Kürti, J.; Rajczy, P.; Kertesz, M.; Hafner, J.; Kresse, G. Performance of the Vienna Ab Initio Simulation Package (VASP) in Chemical Applications. *J. Mol. Struct. THEOCHEM* **2003**, *624* (1–3), 37–45.
(32) Perdew, J. P.; Burke, K.; Ernzerhof, M. Generalized Gradient Approximation Made Simple. *Phys. Rev. Lett.* **1996**, *77* (18), 3865.
(33) Chang, H.-Y.; Kim, S.-H.; Halasyamani, P. S.; Ok, K. M. Alignment of Lone Pairs in a New Polar Material: Synthesis, Characterization, and Functional Properties of Li2Ti (IO3) 6. *J. Am. Chem. Soc.* **2009**, *131* (7), 2426–2427.
(34) Maintz, S.; Deringer, V. L.; Tchougréeff, A. L.; Dronskowski, R. LOBSTER: A Tool to Extract Chemical Bonding from Plane-wave Based DFT. **2016**.

(35) Dronskowski, R.; Bloechl, P. E. Crystal Orbital Hamilton Populations (COHP): Energy-Resolved Visualization of Chemical Bonding in Solids Based on Density-Functional Calculations. *J. Phys. Chem.* **1993**, *97* (33), 8617–8624.
(36) Deringer, V. L.; Tchougréeff, A. L.; Dronskowski, R. Crystal Orbital Hamilton Population (COHP) Analysis as Projected from Plane-Wave Basis Sets. *J. Phys. Chem. A* **2011**, *115* (21), 5461–5466.
(37) Mentré, O.; Juárez-Rosete, M. A.; Saitzek, S.; Aguilar-Maldonado, C.; Colmont, M.; Arévalo-López, Á. M. S= 1/2 Chain in BiVO3F: Spin Dimers versus Photoanodic Properties. *J. Am. Chem. Soc.* **2021**, *143* (18), 6942–6951.
(38) Kubelka, P.; Munk, F. A Contribution to the Optics of Pigments. *Z Tech Phys* **1931**, *12* (593), 193.
(39) Tauc, J.; Grigorovici, R.; Vancu, A. Optical Properties and Electronic Structure of Amorphous Germanium. *Phys. Status Solidi B* **1966**, *15* (2), 627–637.
(40) Wang, V.; Xu, N.; Liu, J.-C.; Tang, G.; Geng, W.-T. VASPKIT: A User-Friendly Interface Facilitating High-Throughput Computing and Analysis Using VASP Code. *Comput. Phys. Commun.* **2021**, *267*, 108033.
(41) Gamon, J.; Giaume, D.; Wallez, G.; Labégorre, J.-B.; Lebedev, O.; Al Rahal Al Orabi, R.; Haller, S.; Le Mercier, T.; Guilmeau, E.; Maignan, A. Substituting Copper with Silver in the BiMOCh Layered Compounds (M= Cu or Ag; Ch= S, Se, or Te): Crystal, Electronic Structure, and Optoelectronic Properties. *Chem. Mater.* **2018**, *30* (2), 549–558.
(42) Silvi, B.; Savin, A. Classification of Chemical Bonds Based on Topological Analysis of Electron Localization Functions. *Nature* **1994**, *371* (6499), 683–686.
(43) Walsh, A.; Payne, D. J.; Egdell, R. G.; Watson, G. W. Stereochemistry of Post-Transition Metal Oxides: Revision of the Classical Lone Pair Model. *Chem. Soc. Rev.* **2011**, *40* (9), 4455–4463.
(44) Payne, D. J.; Egdell, R. G.; Walsh, A.; Watson, G. W.; Guo, J.; Glans, P.-A.; Learmonth, T.; Smith, K. E. Electronic Origins of Structural Distortions in Post-Transition Metal Oxides: Experimental and Theoretical Evidence for a Revision of the Lone Pair Model. *Phys. Rev. Lett.* **2006**, *96* (15), 157403.
(45) Otero-de-la-Roza, A.; Johnson, E. R.; Luaña, V. Critic2: A Program for Real-Space Analysis of Quantum Chemical Interactions in Solids. *Comput. Phys. Commun.* **2014**, *185* (3), 1007–1018.
(46) de-la Roza, A. O.; Blanco, M.; Pendás, A. M.; Luana, V. Critic: A New Program for the Topological Analysis of Solid-State Electron Densities. *Comput. Phys. Commun.* **2009**, *180* (1), 157–166.
(47) Wang, H.; Kohyama, M.; Tanaka, S.; Shiihara, Y. Ab Initio Local Energy and Local Stress: Application to Tilt and Twist Grain Boundaries in Cu and Al. *J. Phys. Condens. Matter* **2013**, *25* (30), 305006.
(48) Walsh, A.; Watson, G. W. Influence of the Anion on Lone Pair Formation in Sn (II) Monochalcogenides: A DFT Study. *J. Phys. Chem. B* **2005**, *109* (40), 18868–18875.
(49) Poupon, M.; Barrier, N.; Petit, S.; Clevers, S.; Dupray, V. Hydrothermal Synthesis and Dehydration of CaTeO3 (H2O): An Original Route to Generate New CaTeO3 Polymorphs. *Inorg. Chem.* **2015**, *54* (12), 5660–5670.
(50) Poupon, M.; Barrier, N.; Petit, S.; Boudin, S. A New β-CdTeO 3 Polymorph with a Structure Related to α-CdTeO 3. *Dalton Trans.* **2017**, *46* (6), 1927–1935.
(51) Ohtani, B. Photocatalysis by Inorganic Solid Materials: Revisiting Its Definition, Concepts, and Experimental Procedures. *Adv. Inorg. Chem.* **2011**, *63*, 395–430.
(52) Leroy, S.; Blach, J.-F.; Huvé, M.; Léger, B.; Kania, N.; Henninot, J.-F.; Ponchel, A.; Saitzek, S. Photocatalytic and Sonophotocatalytic Degradation of Rhodamine B by Nano-Sized La2Ti2O7 Oxides Synthesized with Sol-Gel Method. *J. Photochem. Photobiol. Chem.* **2020**, *401*, 112767. https://doi.org/10.1016/j.jphotochem.2020.112767.
(53) Belver, C.; Adán, C.; Fernández-García, M. Photocatalytic Behaviour of Bi2MO6 Polymetalates for Rhodamine B Degradation. *Catal. Today* **2009**, *143* (3), 274–281. https://doi.org/10.1016/j.cattod.2008.09.011.

(54) Lucid, A.; Iwaszuk, A.; Nolan, M. A First Principles Investigation of Bi2O3-Modified TiO2 for Visible Light Activated Photocatalysis: The Role of TiO2 Crystal Form and the Bi3+ Stereochemical Lone Pair. *Mater. Sci. Semicond. Process.* **2014**, *25*, 59–67.
(55) Iwaszuk, A.; Nolan, M. SnO-Nanocluster Modified Anatase TiO 2 Photocatalyst: Exploiting the Sn (II) Lone Pair for a New Photocatalyst Material with Visible Light Absorption and Charge Carrier Separation. *J. Mater. Chem. A* **2013**, *1* (22), 6670–6677.
(56) Shaikh, S. K.; Inamdar, S. I.; Ganbavle, V. V.; Rajpure, K. Y. Chemical Bath Deposited ZnO Thin Film Based UV Photoconductive Detector. *J. Alloys Compd.* **2016**, *664*, 242–249.
(57) Zhao, Q.; Wang, W.; Carrascoso-Plana, F.; Jie, W.; Wang, T.; Castellanos-Gomez, A.; Frisenda, R. The Role of Traps in the Photocurrent Generation Mechanism in Thin InSe Photodetectors. *Mater. Horiz.* **2020**, *7* (1), 252–262.
(58) Parkinson, B.; Turner, J.; Peter, L.; Lewis, N.; Sivula, K.; Domen, K.; Bard, A. J.; Fiechter, S.; Collazo, R.; Hannappel, T. *Photoelectrochemical Water Splitting: Materials, Processes and Architectures*; Royal Society of Chemistry, 2013.
(59) Hwang, I.; McNeill, C. R.; Greenham, N. C. Drift-Diffusion Modeling of Photocurrent Transients in Bulk Heterojunction Solar Cells. *J. Appl. Phys.* **2009**, *106* (9), 094506.
(60) Zhou, L.; Zhang, H.; Sun, H.; Liu, S.; Tade, M. O.; Wang, S.; Jin, W. Recent Advances in Non-Metal Modification of Graphitic Carbon Nitride for Photocatalysis: A Historic Review. *Catal. Sci. Technol.* **2016**, *6* (19), 7002–7023.
(61) Bott, A. W. Electrochemistry of Semiconductors. *Curr. Sep.* **1998**, *17*, 87–92.
(62) Lin, L.; Lin, J. M.; Wu, J. H.; Hao, S. C.; Lan, Z. Photovoltage Enhancement of Dye Sensitised Solar Cells by Using ZnO Modified TiO2 Electrode. *Mater. Res. Innov.* **2010**, *14* (5), 370–374. https://doi.org/10.1179/143307510X12820854748791.
(63) Butler, M.; Ginley, D. Prediction of Flatband Potentials at Semiconductor-electrolyte Interfaces from Atomic Electronegativities. *J. Electrochem. Soc.* **1978**, *125* (2), 228.
(64) Xu, Y.; Schoonen, M. A. The Absolute Energy Positions of Conduction and Valence Bands of Selected Semiconducting Minerals. *Am. Mineral.* **2000**, *85* (3–4), 543–556.
(65) Castelli, I. E.; Landis, D. D.; Thygesen, K. S.; Dahl, S.; Chorkendorff, I.; Jaramillo, T. F.; Jacobsen, K. W. New Cubic Perovskites for One-and Two-Photon Water Splitting Using the Computational Materials Repository. *Energy Environ. Sci.* **2012**, *5* (10), 9034–9043.
(66) Allen, J. P.; Carey, J. J.; Walsh, A.; Scanlon, D. O.; Watson, G. W. Electronic Structures of Antimony Oxides. *J. Phys. Chem. C* **2013**, *117* (28), 14759–14769.
(67) Shi, Y.-F.; Li, X.-F.; Zhang, Y.-X.; Lin, H.; Ma, Z.; Wu, L.-M.; Wu, X.-T.; Zhu, Q.-L. [(Ba19Cl4)(Ga6Si12O42S8)]: A Two-Dimensional Wide-Band-Gap Layered Oxysulfide with Mixed-Anion Chemical Bonding and Photocurrent Response. *Inorg. Chem.* **2019**, *58* (10), 6588–6592.
(68) Ogisu, K.; Ishikawa, A.; Shimodaira, Y.; Takata, T.; Kobayashi, H.; Domen, K. Electronic Band Structures and Photochemical Properties of La− Ga-Based Oxysulfides. *J. Phys. Chem. C* **2008**, *112* (31), 11978–11984.
(69) Carey, J. J.; Allen, J. P.; Scanlon, D. O.; Watson, G. W. The Electronic Structure of the Antimony Chalcogenide Series: Prospects for Optoelectronic Applications. *J. Solid State Chem.* **2014**, *213*, 116–125.
(70) Hu, C.; Mutailipu, M.; Wang, Y.; Guo, F.; Yang, Z.; Pan, S. The Activity of Lone Pair Contributing to SHG Response in Bismuth Borates: A Combination Investigation from Experiment and DFT Calculation. *Phys. Chem. Chem. Phys.* **2017**, *19* (37), 25270–25276.
(71) Yin, R.; Hu, C.; Lei, B.-H.; Pan, S.; Yang, Z. Lone Pair Effects on Ternary Infrared Nonlinear Optical Materials. *Phys. Chem. Chem. Phys.* **2019**, *21* (9), 5142–5147.
(72) Orr, M.; Hebberd, G. R.; McCabe, E. E.; Macaluso, R. T. Structural Diversity of Rare-Earth Oxychalcogenides. *ACS Omega* **2022**.

For Table of Contents Only